Nanoscale Advances

ROYAL SOCIETY OF CHEMISTRY

PAPER

View Article Online
View Journal | View Issue

Cite this: *Nanoscale Adv.*, 2023, **5**, 3521

Direction- and polarization-tunable spontaneous emission beneficial from diffraction orders of a square R6G-nanopore array†

Shijia He,[ab] Yi Wang,*[ab] Tianyu Wang,[b] Dongda Wu,[ab] Junqiao La,[ab] Jiang Hu,[b] Jiamin Xiao[b] and Wenxin Wang *[ab]

Received 14th March 2023
Accepted 4th June 2023

DOI: 10.1039/d3na00160a

rsc.li/nanoscale-advances

To meet the miniaturization and compatibility of current micro-nano optical devices, two-dimensional (2D) photonic crystals (PCs), which can manipulate the optical parameters and their propagation with more degree of freedom, have become more important in nano optics. In the case of 2D PCs, the specific symmetry of the microscopic lattice arrangement determines its macroscopic optical properties. In addition, beyond this key element of lattice arrangement, the unit cell of PCs is also a critical factor in modulating the far-field optical behaviors. This work explores the manipulation of spontaneous emission (SE) of rhodamine 6G (R6G) in a square lattice of anodic aluminum oxide (AAO) membrane. The directional and polarized emissions are observed to be related to the diffraction orders (DOs) of the lattice arrangement. By further tuning the size of unit cells, different DOs are triggered to overlap with the emission of R6G, resulting in an extended tuning for directions and polarizations of light emission. It exhibits the significance for the design and application of nano optics devices.

Introduction

Photons, instead of electrons, are treated as attractive information carriers to meet the increasing demands from high efficiency, low loss, and fast speed to high data capability in information processing.[1] How to tune the optical parameters easily and flexibly become particularly important, for instance, polarization states,[2–5] intensity enhancement and resonance energy variation.[6–8] Two-dimensional (2D) photonic crystals (PCs), as an artificial periodic structure,[9,10] have attracted extensive attention from the scientific community due to their flexibility and controllability in light regulation.[11,12] They show significant promise in holographic imaging,[13] polarization imaging,[14–16] optical communication,[17,18] and optical sensing application potential[19,20] because of the far-field diffraction in 2D PCs. Therefore, the desired appealing optical parameters can be achieved through the elaborate design of 2D PCs, especially for structural symmetry and the unit cell design.[21]

As an optical micro cavity composed of sub-wavelength scale resonators, 2D PCs possess the ability to tune the spontaneous emission (SE) of inside emitters because of the Purcell effect.[22] Since Goy *et al.* first observed the regulation and enhancement of SE by optical cavities in the 1980s, more attention to light–matter interaction in optical cavities has been widely concerned.[23] Amplification of emission intensity is a typical topic for the SE modulation,[24,25] but it is worth noting that the directional and polarized emissions are also productive for the further application of quantum emitters. In order to realize more tunable control of optical parameters, the eigenmodes of optical cavities with periodic nanostructure arrangement should be investigated. The intrinsic optical properties of 2D PCs are closely interrelated with structural characteristics, such as the symmetry of lattice arrangement and the size and components of the unit cell.[26–28] Thereinto, the far-field diffraction orders (DOs) depending on the symmetry of lattice arrangement play a key role in analyzing the interaction between light and matter in different directions and polarizations effectively;[29] on top of that, the size of the unit cell provides a better-matched resonance energy for the system between the emitters and the optical cavity.

Here, a square lattice anodized aluminum oxide (AAO) membrane with a period of 400 nm was prepared as an optical cavity to tune the SE properties of rhodamine 6G (R6G). First, the Γ point energy (560 nm) of AAO was tuned to match and adjust the dominant isotropic photoluminescence (PL) of R6G into a polarization-resolved normal emission. Since this Γ point was a degenerate state of four DOs modes, an off-angle (6°) PL measurement was applied to lift it into two singlet modes of (−1, 0) and (1, 0), and a doublet mode of (0, 1)/(0, −1). Interestingly, the PL of R6G presents obviously directional and polarized distinguished emission as its spectral overlapping

[a]College of Physics and Optoelectronic Engineering, Harbin Engineering University, 150001 Harbin, China. E-mail: yi.wang@hrbeu.edu.cn; wenxin.wang@hrbeu.edu.cn
[b]Qingdao Innovation and Development Center of Harbin Engineering University, Harbin Engineering University, 266500 Qingdao, China

† Electronic supplementary information (ESI) available. See DOI: https://doi.org/10.1039/d3na00160a

with the (0, 1)/(0, −1) mode at 554 nm and (−1, 0) mode at 582 nm. Finally, both DOs were adjusted to sequentially couple with the central peak of R6G emission at 560 nm through the diameter-tuning of the unit cell. This work paves the way for the application of AAO as 2D PCs in optical switches, nanolasing, and quantum information.

Results and discussions

Fig. 1a schematic depicts the preparation process of the AAO membrane covered with R6G. By imprinting a predetermined periodic pattern on a polished aluminum foil, an ordered AAO membrane with a period of 400 nm and internal pore size of 240 nm is obtained by the anodization and pore expanding processes. Then, the R6G aqueous solution is packaged on the surface of AAO by a liquid-encapsulated technique, as shown in Fig. S1.† The $\mathbf{a_1}$ and $\mathbf{a_2}$ (black arrows) are primitive vectors of the square lattice in real space, which can be described as $|\mathbf{a_1}| = |\mathbf{a_2}| = a$, a is the lattice constant of the square lattice. The scanning electron microscope (SEM) image of AAO with detailed lattice parameters is displayed in Fig. 1b; the inserted top image with a perspective view illustrates the detailed profile feature of the pore structure, and the bottom image shows the effective sample diameter that reaches 1 cm. The corresponding square lattice in reciprocal space is shown in Fig. 1c. The reciprocal lattice vectors can be expressed as $\mathbf{G_{ij}} = i\mathbf{b_1} + j\mathbf{b_2}$, where $\mathbf{b_1}$ and $\mathbf{b_2}$ (black arrows) are primitive vectors of the square lattice in reciprocal space and their magnitude can be described as $|\mathbf{b_1}| = |\mathbf{b_2}| = 2\pi/a$, i and j are integers. The $\mathbf{k_{//}}$ is the in-plane wavevector component that is parallel to the lattice surface. The wave vector of DOs, $\mathbf{k_{DO}}$, can be indicated as $\mathbf{k_{DO}} = \mathbf{G_{ij}} + \mathbf{k_{//}}$. The first Brillion Zone (1st BZ) is exhibited as a dark blue area, and the high symmetry points are denoted as Γ, X, and M points, respectively.

Under the normal incidence, the four lowest DOs in reciprocal space have the same magnitude and meet at the Γ point as a degenerated state. In the case of oblique incidence, a non-zero in-plane wave vector $\mathbf{k_{//}}$ should be considered. For instance, the (0, 1) and (0, −1) DOs have the same magnitude and maintain the degenerated state, but the (1, 0) and (−1, 0) DOs possess different magnitudes and divide into higher and lower photonic energy levels, respectively. The reflection of AAO (red curve) and the PL emission of R6G (blue curve) are plotted in the left panel of Fig. 1d. The diffraction energy of DOs is tuned to match the dominant PL emission of R6G. The reflection dispersion of AAO in the aqueous solution (refractive index of 1.33) is exhibited as a function of the emission angle along the Γ–X orientation in the right panel of Fig. 1d. In the off-angle condition, the degenerate mode will be lifted as the (0, ±1) modes in the red curve, the (−1, 0) mode in the navy-blue curve, and the (1, 0) mode in the green curve. The dashed lines are the numerical

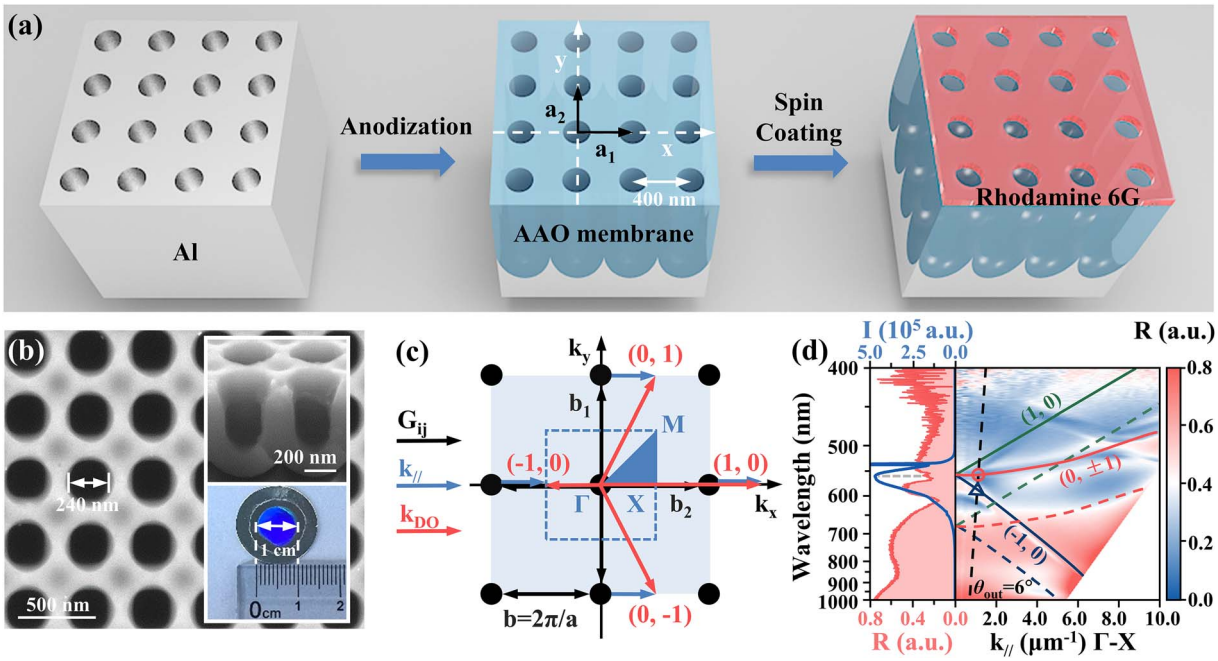

Fig. 1 The large-area AAO nanopore array in real space and reciprocal space. (a) Schematic diagram of the preparation process for AAO covered by R6G with lattice constant a = 400 nm, $\mathbf{a_1}$ and $\mathbf{a_2}$ are the primitive vectors in the real space lattice. (b) Top-view SEM image of AAO with a pore diameter of 240 nm (insert: perspective view and optical image of AAO). The scale bar is 500 nm. (c) The reciprocal lattice (light blue area) corresponds to the real lattice, and the reciprocal lattice vectors are $\mathbf{b_1}$ and $\mathbf{b_2}$ (black arrows). The dark blue area signifies the 1st BZ. The three vertices of the dark blue triangle are high symmetry points of Γ, M and X. $\mathbf{G_{ij}}$ is the reciprocal lattice vector. $\mathbf{k_{//}}$ (dark blue arrow) is the in-plane incident wavevector. $\mathbf{k_{DO}}$ (red arrow) is a wavevector of the diffraction order. The green arrow exhibits the electric polarization for TE mode. (d) Left panel: the reflection spectrum of AAO (red curve) and PL emission of composite R6G-water (blue curve) at 0° emission angle. Right panel: the experimental angular-resolved spectra of AAO with R6G-water. The green, red, and blue lines indicate the DOs of (1, 0), (0, ±1), and (−1, 0), respectively. The solid lines are the actual measurement data, and the dotted lines are the approximate simulation calculation data by the ELA method.

calculated DOs by the empty lattice approximation (ELA) method.

Fig. 2a depicts a schematic diagram of the measurement setup of the angle-resolved spectrum, θ_{in} denotes the incident angle, θ_{out} is the emission angle, and φ is the azimuth angle. The measured transmitted signal is coupled to the optical fiber through the mirror and collimator and sent to the spectrometer for analysis. After spectral overlapping with the degenerate states of AAO at Γ point, the PL spectrum of R6G after difference processing is demonstrated in the left panel of Fig. 2b, which is spectrally enhanced at 560 nm in the range from 540 to 640 nm. Its PL dispersion as a function of emission angle from 0° to 30° under the driving light of 532 nm is exhibited in the right panel.

A comparison of R6G emission on Al foil and the AAO membrane also proves the modulation effect of the square lattice in Fig. S2.† Benefiting from diffraction orders of square R6G-nanopore array, the emission intensity of R6G is enhanced about 1.4-fold compared with that on Al foil at $\theta_{out} = 0°$. As expected, the PL of R6G at Γ point of AAO exhibits obvious polarization-dependent emission, and the emission polarization angle (θ_p) is 45°, as shown in Fig. 2c, where the isotropic emission from R6G on blank Al foil is plotted in gray as reference. The polarization-dependent emission of R6G can be well-fitted by a typical angular function of electric dipole resonances. The function can be defined as $A\cos^4(\alpha - \alpha_0) + B\cos^4(\alpha - \alpha_1)$, where α is the polarization angle, α_0 and α_1 are two constants of the fitting.[30] Similarly, a 45° polarization reflection is achieved under a white light source in Fig. S3.† This phenomenon should relate to the local density of states and the symmetry of the square lattice and can be regulated by the degenerated states of DOs.

Since the Γ point is a four-fold degenerated state with a C_{4v} symmetry, singlet or low-fold doublet states are required to analyze the symmetry-related optical parameters, such as polarization. In the case of the off-angle condition, as shown in the right panel of Fig. 2b, the degenerate mode will be lifted as a doublet mode of (0, ±1) in the red curve and a singlet mode of (−1, 0) in the navy-blue curve as ELA prediction. In order to keep the intersecting of resonant (0, ±1) and (−1, 0) DOs with the PL emission of R6G in the range from 540 nm to 640 nm, a representative measurement is taken out at $\theta_{out} = 6°$, which can promise the distinguished PL peaks in relative high intensity. Interestingly, the PL emission behaves horizonal-polarization dependent ($\theta_p = 0°$) as it couples to the (0, ±1) mode (red color) in Fig. 2d. The PL emission performs vertical-polarization dependent ($\theta_p = 90°$) as it couples to the (−1, 0) mode (blue color). The difference in polarization degree between the two signals is analyzed in Fig. S4.† The same polarization conditions occur with reflection spectra of the square lattice AAO under a white light source in Fig. S5.†

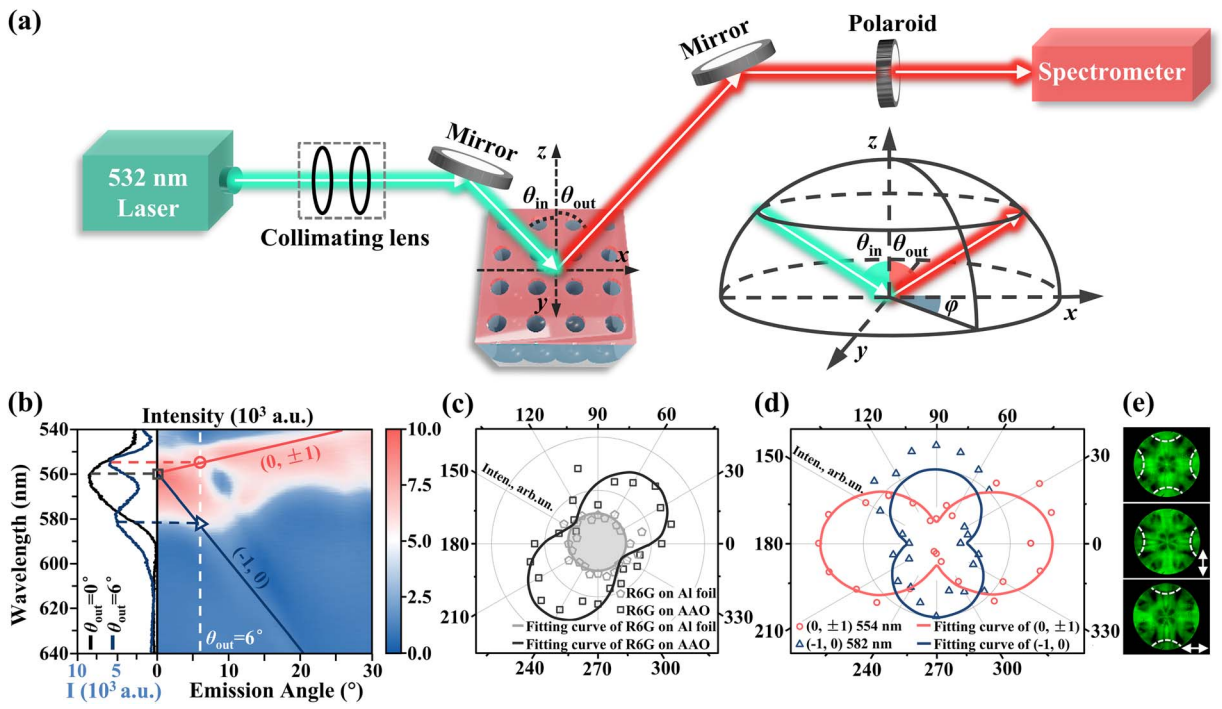

Fig. 2 SE regulation of R6G by AAO nanopore array. (a) Schematic diagram of angle-resolved measurement setup for the AAO nanopore array (inset: spatial schematic diagram of incident angle θ_{in}, emission angle θ_{out}, and azimuth angle φ. The incident light and the emission light are located at the same plane). (b) Left panel: the PL spectrum of R6G under the incident angle of 0° (black line) and 6° (blue line), respectively. Right panel: PL dispersion as a function of emission angle from 0° to 30° under the driving light of 532 nm, in which the white dotted line represents the emission angle of 6°, the red and blue solid lines indicate the DOs of (0, ±1) and (−1, 0), respectively. (c) Polarization of R6G normal emission on Al foil (gray) and AAO membrane (black). (d) The off-angle SE (6°) of R6G as a function of polarization at 554 nm (red) and 582 nm (blue), respectively. (e) The optical Fourier images collected at the back focal plane of the objective lens under driving light of 560 nm without polarizer (the top image) and with orthogonal polarizers (the middle and the bottom images).

In order to further explain the underlying physics of this performance, a Fourier image system is built to exhibit the light propagation in reciprocal space, and its schematic optical path is shown in Fig. S6.† The Fourier image is captured on the Fourier back plane (FBP) under a driving light of 560 nm without polarizer in the top image of Fig. 2e, and four DOs with white dash lines can be observed with a radius of $\mathbf{k}_{//}$ ($2\pi/\lambda$). In the case of the FBP image with vertical polarizer, (1, 0) and (−1, 0) modes can be observed in the middle image of Fig. 2e. On the other hand, only the (0, ±1) DOs can be obtained with the horizonal polarizer, as exhibited in the bottom image of Fig. 2e. The DOs can be observed when the dipolar radiative direction in the lattice is perpendicular to the polarization of incident light.[31] Since there are four equivalent DOs degenerated at Γ point (under normal incidence) in square photonic lattice, only two DOs appear in either horizonal or vertical polarization.

In addition, the polarization characteristics of the two signals can be further explained by the group theory, where two-dimensional square lattice obeys C_{4v} symmetry and the optical parameters of corresponding DOs, for instance, polarization, propagation direction *etc.*, can be described by particular irreducible representation.[32] In this work, the irreducible representation of the doublet (0, ±1) mode is E or A + B and that of the singlet (−1, 0) mode is A;[33] therefore, both modes possess different symmetry operations and polarization-dependence. Normally, the luminescence of R6G is a SE without directional and polarization dependence. In this work, the far-field emission from the R6G packaged on the square photonic lattice presents a particular polarization characteristic because the measured emission is a hybrid mode that possesses the properties from both eigenmodes when R6G emission couples with the resonant DO mode.

Based on the polarization-resolved characteristics of SE on the square lattice, the energy of DOs is regulated to couple with the emission peak of R6G. The directional and polarized emission behavior of R6G strongly correlates with the intrinsic optical properties of 2D PCs. In this optical cavity of AAO membrane with the square lattice, the diameter of the unit cell is another critical determinant for varying the resonant energy of the DOs, which can be flexibly controlled by chemical wet etching. The variation in pore diameters can be clearly observed in SEM images in Fig. S7.† As presented in Fig. 3a, the degenerated energy of Γ point can be extended into a flexible spectral range from 1.99 eV to 2.51 eV, where the energy of Γ point increases with the pore diameter. For instance, it increases from 2.12 eV (585 nm) to 2.31 eV (536 nm) when the pore diameter expanded from 220 nm to 300 nm, as shown in the inset of Fig. 3a. The experimental and simulated angular-resolved dispersions of AAO membranes with various diameters further illustrate the shift of DOs in Fig. S8 and S9,† respectively.

In addition, the variation tendency of the dominant emission wavelength of R6G is well consistent with DOs, as shown in Fig. S10,† indicating the modulation effect of square lattice on the SE of R6G. Particularly, the DOs of (0, ±1) in red and (−1, 0) in blue are sequentially coupled to the central emission of R6G (560 nm) at $\theta_{out} = 23°$ and $\theta_{out} = 5°$, respectively, in Fig. 3b.

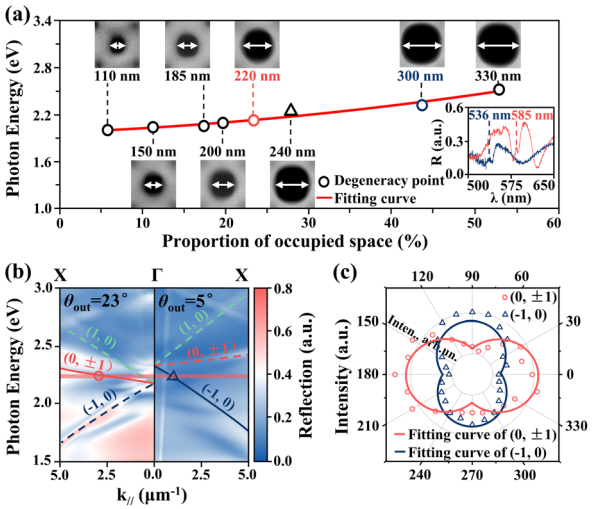

Fig. 3 Modulating of the unit cell size of AAO nanopore array and its effect on the polarization of R6G emission. (a) The relationship between the energy of Γ point and the occupied proportion of pore space, the red solid line denotes the fitting curve (inset: comparison of spectra of AAO nanopore array with different diameters at $\theta_{out} = 0°$). (b) Experimental angular-resolved dispersions of nanopore arrays with diameters of 220 nm (left panel) and 300 nm (right panel), the corresponding θ_{out} are 23° and 5° when the DOs overlap with the central emission of R6G, respectively. (c) Polarization of R6G emission generated on the above two AAO membranes at 560 nm, the predominant DOs are (0, ±1) of red color and (−1, 0) of blue color, respectively.

There is a 90° difference in polarization under the effect of two DOs, as presented in Fig. 3c, which has the same trend of polarization characteristics as described in Fig. 2d. This ability to regulate polarizations at the specific wavelength comes from the far-field DOs and flexible spectral range of the square lattice, as illustrated in Fig. S11.†

Conclusions

In conclusion, a directional and polarized SE was modulated on a square lattice of AAO membrane with R6G. The PL emission of R6G presents an obvious polarization-related property due to its energy coupling with DOs of AAO at Γ point, which verifies that the local density of states and symmetry of the square lattice play a key effect on the regulation of optical parameters of SE from emission direction, wavelength, intensity to polarization states. An off-angle PL measurement was applied to lift the four-fold degenerated DOs into a doublet mode of (0, ±1) and two singlet modes of (1, 0) and (−1, 0), which behave as the horizonal- and vertical-related polarizations, respectively. In addition, the energy of DOs can be further extended by varying the diameter of the unit cell, which results in a flexible energy range from 1.99 eV to 2.51 eV. After spectral overlapping of (0, ±1) and (−1, 0) DOs with the central peak of R6G at 560 nm, emissions from the two states exhibit a 90° dissimilarity in polarization. Therefore, this work has great potential in the field of the optical switch device, nanolasing, and quantum information.

Experimental section

Preparation of AAO membrane

By imprinting a predetermined pattern on polished aluminum foil and further anodizing in a mixture of aqueous solution of phosphoric acid and ethylene glycol, a large-area ordered AAO membrane with a period of 400 nm can be achieved. Under the condition of the water bath at 55 °C, 5 wt% phosphoric acid is used to expand the pores of AAO membranes at different time periods; for instance, the pore-expanding time is 14 min for the AAO membrane of 330 nm diameter.

Packaging R6G with AAO membrane

R6G is packaged on AAO membranes in a liquid-encapsulated manner. The R6G aqueous solution (80 mg R6G added into 50 mL water) is uniformly applied to the surface of AAO membranes by dropwise addition, which is placed on the slide. A coverslip is placed on its surface to completely immerse the sample in R6G aqueous solution, and the edges are fixed using adhesive tape. The AAO membranes can be viewed as immersed in a homogeneous refractive index environment, which is essential for achieving superior luminescence.

Angle-resolved reflection measurement

Zero-order reflection spectra are measured using an automatic rotating stage from 0° to 60° in increments of 1° at a fixed azimuth angle. The sample is illuminated using a white light source from a halogen lamp (iDH2000, Ideaoptics) with a polarizer, where the illumination spot on the sample is 1–2 mm in diameter. The reflected light is collected and coupled to an optical fiber which is connected to a fiber spectrometer (PG 2000, Ideaoptics). An algorithm is used to convert the measured optical data (wavelength *vs.* polar angle) into a dispersion diagram (photon energy E *vs.* in-plane wavevector of light $\mathbf{k}_{//}$).

A random polarization laser of 532 nm (Lasever, LSR532HX-5W) is applied as an excitation light to investigate the emission and polarization-dependent properties of R6G. The laser spot size is around 1 mm, and the pumping energy is 2 W.

Simulation calculations

Finite-different time-domain (FDTD Solutions, ANSYS) is used to simulate the intrinsic optical properties of AAO membranes in Fig. S9.† The simulation model of AAO membranes is emanated from the structural data of SEM images. The plane wave (BFAST) and Bloch (x, y)-PML (z) are used as the boundary condition for the E–$\mathbf{k}_{//}$ dispersion diagram simulations.

Author contributions

Shijia He, Yi Wang and Wenxin Wang designed the study and performed the research. Shijia He and Tianyu Wang fabricated the samples. Shijia He wrote the original draft, and Wenxin Wang and Yi Wang supervised the project and developed the manuscript. Junqiao La helped in experimental data discussion and analysis. Dongda Wu, Jiang Hu and Jiamin Xiao helped with the Fourier imaging. All authors contributed to the scientific discussions and paper revisions.

Conflicts of interest

There are no conflicts to declare.

Acknowledgements

The authors would like to thank Xuchao Zhao and Ye Xiang of Qingdao Innovation and Development Center of Harbin Engineering University for helpful discussions on topics related to this work. This work was financially supported by the National Natural Science Foundation of China (No. 61905049 and 61905051), the Natural Science Foundation of Heilongjiang Province (LH2020A007 and LH2020F027), and the Fundamental Research Funds for the Central Universities (3072022TS2613).

References

1 Y. A. Vlasov, X. Bo, J. C. Sturm and D. J. Norris, *Nature*, 2001, **414**, 289–293.
2 M. D. Turner, M. Saba, Q. Zhang, B. P. Cumming, G. E. Schröder-Turk and M. Gu, *Nat. Photonics*, 2013, **7**, 801–805.
3 E. Mogni, G. Pellegrini, J. Gil-Rostra, F. Yubero, G. Simone, S. Fossati, J. Dostálek, R. Martínez Vázquez, R. Osellame, M. Celebrano, M. Finazzi and P. Biagioni, *Adv. Opt. Mater.*, 2022, **10**, 2200759.
4 F. Xia, H. Wang, D. Xiao, M. Dubey and A. Ramasubramaniam, *Nat. Photonics*, 2014, **8**, 899–907.
5 Y. Zhang, A. Chen, W. Liu, C. Hsu, B. Wang, F. Guan, X. Liu, L. Shi, L. Lu and J. Zi, *Phys. Rev. Lett.*, 2018, **120**, 186103.
6 S. Hu, H. Xu, B. Zhou, S. Xu, B. Shen, B. Dong, Z. Yin, S. Xu, L. H. Sun, J. K. Lv, J. H. Wang, W. Xu, X. Bai, L. Xu, S. Mintova and H. W. Song, *Sens. Actuators, B*, 2021, **326**, 128816.
7 Y. Liang, Z. Wang, J. Wolf, E. Gini, M. Beck, B. Meng, J. Faist and G. Scalari, *Appl. Phys. Lett.*, 2019, **114**, 031102.
8 S. Shahid, S. E. Zumrat and M. A. Talukder, *Nanoscale Adv.*, 2022, **4**, 801–813.
9 C. Fenzl, T. Hirsch and O. S. Wolfbeis, *Angew. Chem., Int. Ed.*, 2014, **53**, 3318–3335.
10 W. Zhou, D. Zhao, Y. Shuai, H. Yang, S. Chuwongin, A. Chadha, J. Seo, K. X. Wang, V. Liu, Z. Ma and S. Fan, *Prog. Quantum Electron.*, 2014, **38**, 1–74.
11 Y. Wang, F. Lv, J. Chen, Y. Huang, S. He, W. Xu, S. Xu and W. Wang, *ACS Appl. Mater. Interfaces*, 2021, **13**, 47262–47271.
12 F. H. L. Koppens, T. Mueller, P. Avouris, A. C. Ferrari, M. S. Vitiello and M. Polini, *Nat. Nanotechnol.*, 2014, **9**, 780–793.
13 G. Yoon, D. Lee, K. T. Nam and J. Rho, *ACS Nano*, 2018, **12**, 6421–6428.
14 A. Chen, W. Liu, Y. Zhang, B. Wang, X. Liu, L. Shi, L. Lu and J. Zi, *Phys. Rev. B*, 2019, **99**, 180101.
15 R. Zhao, G. Geng, Q. Wei, Y. Liu, H. Zhou, X. Zhang, C. He, X. Li, X. Li, Y. Wang, J. Li and L. Huang, *Adv. Opt. Mater.*, 2022, **10**, 2102596.

16 F. Yesilkoy, E. R. Arvelo, Y. Jahani, M. Liu, A. Tittl, V. Cevher, Y. Kivshar and H. Altug, *Nat. Photonics*, 2019, **13**, 390–396.
17 F. Mehdizadeh, M. Soroosh and H. Alipour-Banaei, *Optik*, 2016, **127**, 8706–8709.
18 F. Gao, H. Xue, Z. Yang, K. Lai, Y. Yu, X. Lin, Y. Chong, G. Shvets and B. Zhang, *Nat. Phys.*, 2018, **14**, 140–144.
19 Z. Fu, J. Zhou, L. Huang, F. Sun and H. Tian, *Opt. Commun.*, 2016, **381**, 146–151.
20 R. Sakata, K. Ishizaki, M. De Zoysa, S. Fukuhara, T. Inoue, Y. Tanaka, K. Iwata, R. Hatsuda, M. Yoshida, J. Gelleta and S. Noda, *Nat. Commun.*, 2020, **11**, 3487.
21 S. R. Cornelious, T. Sahoo, A. Sujatha and P. Chelliah, *Opt. Commun.*, 2019, **450**, 22–27.
22 S. Wu, S. Buckley, J. R. Schaibley, L. Feng, J. Yan, D. G. Mandrus, F. Hatami, W. Yao, J. Vučković, A. Majumdar and X. Xu, *Nature*, 2015, **520**, 69–72.
23 P. Goy, J. M. Raimond, M. Gross and S. Haroche, *Phys. Rev. Lett.*, 1983, **50**, 1903–1906.
24 M. Pelton, *Nat. Photonics*, 2015, **9**, 427–435.
25 S. Noda, M. Fujita and T. Asano, *Nat. Photonics*, 2007, **1**, 449–458.
26 K. Alnasser, S. Kamau, N. Hurley, J. Cui and Y. Lin, *Photonics*, 2021, **8**, 408.
27 J. Xue, Z. Zhou, L. Lin, C. Guo, S. Sun, D. Lei, C. Qiu and X. Wang, *Light Sci. Appl.*, 2019, **8**, 101.
28 J. Li, Z. Wei, J. Xu, Z. Zhou, D. Kong, J. Liu, J. Liu, X. Duan, J. Xue, J. Wang and X. Wang, *Adv. Opt. Mater.*, 2015, **3**, 1355–1361.
29 S. Kasani, K. Curtin and N. Wu, *Nanophotonics*, 2019, **8**, 2065–2089.
30 Y. Zheng, J. M. Yi, W. X. Wang, M. Silies, Y. F. Zhang, C. Lienau and Y. Lei, *ACS Appl. Nano Mater.*, 2021, **4**, 11563–11572.
31 R. Guo, T. K. Hakala and P. Törmä, *Phys. Rev. B*, 2017, **95**, 155423.
32 M. S. Dresselhaus, G. Dresselhaus and A. Jorio, *Group Theory Application to the Physics of Condensed Matter*, Springer-Verlag, Berlin, 2007.
33 R. Guo, M. Nečada, T. K. Hakala, A. I. Väkeväinen and P. Törmä, *Phys. Rev. Lett.*, 2019, **122**, 013901.